ChemComm

Polypyrrole–polyoxometalate/reduced graphene oxide ternary nanohybrids for flexible, all-solid-state supercapacitors†

Yuyun Chen,‡ Min Han,‡ Yujia Tang, Jianchun Bao, Shunli Li, Yaqian Lan* and Zhihui Dai*

Novel polypyrrole–polyoxometalate/reduced graphene oxide ternary nanohybrids (TNHs) are synthesized *via* a one-pot redox relay strategy. The TNHs exhibit high areal specific capacitance (2.61 mF cm^{-2}), and the fabricated solid device also exhibits good rate capability, excellent flexibility and mechanical stability.

To address global energy and environmental challenges, considerable efforts have been devoted to developing renewable energy and related energy storage and conversion devices.[1,2] Supercapacitors (SCs), also known as electrochemical capacitors, are some of the most promising energy storage devices due to their higher power density, longer lifespan, and better safety tolerance than batteries.[3,4] Recently, flexible and thin SCs (including devices capable of being rolled up) have attracted much attention due to the ever-increasing requirements for lightweight portable electronic devices or wearable electronic products.[5,6] For this purpose, it is important to find proper electro-active materials and integrate them into a special device configuration. Generally, active materials with high specific surface areas, good conductivities, high porosities or tubular or laminar structures are used because they facilitate electron or ion transport, which results in the improvement of the energy storage performance of the desired SCs.[7] Based on the related energy storage mechanism, the currently developed electro-active materials for SCs can be classified into two categories. The first category consists of an electrical double layer of active materials, which generally contains various carbon materials (*e.g.* carbon nanofibers,[8] nanotubes,[9] and 3D graphene (G) frameworks).[10] The second category consists of pseudo-capacitive active materials,

including some metal oxides (*e.g.* MnO_x),[11] hydroxides [*e.g.* β-Co(OH)$_2$ and Ni(OH)$_2$],[12] chalcogenides (*e.g.* VS_2 and MoS_2),[13] and some conducting polymers.[14] As a monolayer of sp^2 hybridized carbon atoms, G possesses a very high theoretical surface area, good electrical conductivity, and excellent mechanical properties, making it a promising active material for SCs, especially for flexible, all-solid-state SCs.[15,16] However, when using G as an active material, only an electrical double layer capacitance can be provided. Moreover, G sheets easily re-stack, which decreases their surface area available for energy storage. Thus, the potential application of G for use in SCs can't be fully realized. To overcome these limitations, it may be feasible to use G as an ideal platform for integrating other pseudo-capacitive materials to form a hybrid electrode.[17,18]

Some pseudo-capacitive materials including metal oxides and conducting polymers have been integrated onto G to form binary nanohybrids and have been applied in SCs.[19–21] Although enhanced specific capacitance, rate capability and cycling stability have been observed in those binary nanohybrids, their energy storage densities are still lower than that of common batteries, and so they need to be further improved. Other than constructing asymmetric SCs and selecting an appropriate organic electrolyte, fabricating ternary nanohybrids (TNHs) by increasing pseudo-capacitive units and optimizing their contact as well as spatial arrangement may be another feasible avenue to improve the energy density of G-based electrode materials. Usually, introducing an additional constituent will pose a great challenge in the synthesis and structural optimization. Though some TNHs containing G or reduced graphene oxide (rGO), metal oxide and conducting polymers have been reported,[22,23] their synthetic processes are complex, time- and energy-consuming, and not environmentally friendly (hazardous agents are often used).[24,25] Thus, exploring a facile strategy to fabricate novel G-based TNHs and improving their energy density are necessary. This is not only important for fundamental study but also for developing high-performance flexible power supply for applying in wearable electronics or nanodevices.

Jiangsu Key Laboratory of Biofunctional Materials, School of Chemistry and Materials Science, Nanjing Normal University, Nanjing 210023, P. R. China. E-mail: daizhihuii@njnu.edu.cn, yqlan@njnu.edu.cn; Fax: +86-25-85891051; Tel: +86-25-85891051
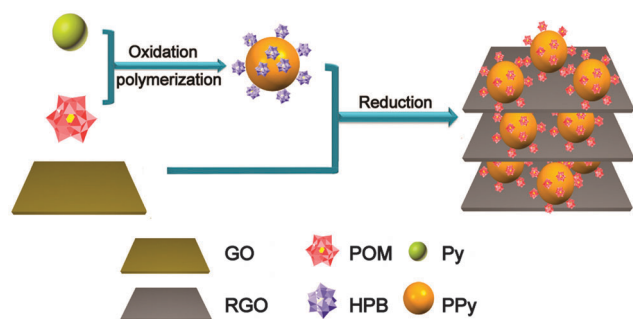
Here, we report the synthesis of novel polypyrrole (PPy)–polyoxometalate ($H_3PMo_{12}O_{40}$, PMo_{12})/rGO TNHs *via* a PMo_{12}-mediated one-pot redox relay strategy and their applications for flexible, all-solid-state SCs (SSCs). As one of the typical polyoxometalates, PMo_{12} has a strong oxidative ability in the acid form and its reductive product, heteropoly blue'' (HPB),[26] possesses a certain reductive ability.[27] It is chosen as a unique multifunctional reagent for initiation of the polymerization reaction of the pyrrole monomer[28] and simultaneous reduction of the chemical oxidation exfoliated GO to rGO by the generated HPB.[29] The polymerization and reductive reactions are triggered by one objective component, PMo_{12}, and no additional oxidant or reductant is involved. Thus, the synthetic process is green, economical, safe and highly efficient.

To the best of our knowledge, this is the first example of using a facile "redox relay" strategy to obtain PPy–PMo_{12}/rGO TNHs. The schematic diagram for formation of such TNHs is given in Scheme 1. In the nanohybrids, the PPy–PMo_{12} nanoparticles are uniformly anchored on the surfaces of the formed rGO nanosheets, which not only alleviate the re-stacking problem of rGO to a certain degree but also create a large amount of mesopores that provide special "highways" for ion diffusion and electron transport. In addition, besides the key role in the synthesis, PMo_{12} components also offer a certain pseudo-capacitance. Thus, the resulting TNHs exhibit much higher specific capacitance than pure rGO and PPy/rGO. Based on these results, the flexible SSCs are further fabricated in a stacked configuration by using polyvinyl alcohol (PVA)/H_2SO_4 gel as a separator and solid electrolyte. At a current density of 150 mA m^{-2}, the areal specific capacitance of the solid device can reach 2.61 mF cm^{-2}. In addition to the high areal specific capacitance, the device also possesses excellent flexibility and mechanical stability, good rate capability and cycling stability, indicating that PPy–PMo_{12}/rGO TNHs are promising active materials for applying in flexible, all-solid-state SCs.

The compositions of the as-synthesized PPy–PMo_{12}/rGO TNHs are firstly characterized by Raman scattering, powder X-ray diffraction (XRD) and Fourier transform infrared (FT-IR) spectroscopy, as shown in the ESI† (Fig. S1). Those spectral data demonstrate that PPy and PMo_{12} have been successfully integrated onto rGO to form the desired TNHs. Further evidence comes from X-ray photoelectron spectroscopy (XPS) analysis.
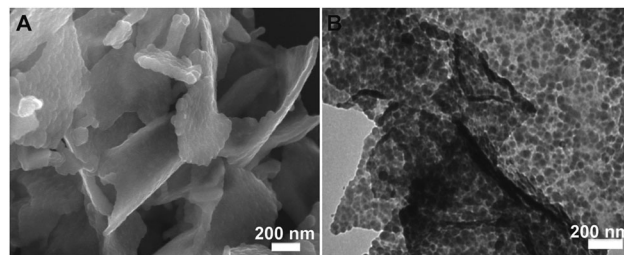

Fig. 1 (A) FE-SEM images of as-synthesized PPy–PMo_{12}/rGO TNHs. (B) TEM images of PPy–PMo_{12}/rGO TNHs.

The XPS spectrum (Fig. S2A, ESI†) shows that the main elements present in the sample are Mo, P, O, C and N. The related fine XPS spectrum of Mo 3d (Fig. S2B, ESI†) confirms that the valence state of Mo is mainly +VI. Combined with the fine XPS spectrum of P 2p (Fig. S2C, ESI†) and O 1s (Fig. S2D, ESI†), the presence of the PMo_{12} component can be verified. Additionally, by deconvoluting the fine XPS spectrum of C 1s (Fig. S2E, ESI†) and N 1s (Fig. S2F, ESI†), the decrease in the number of oxygen-containing groups and the presence of C–N and pyrrole N components further prove the presence of rGO and PPy in the obtained nanohybrids. The shapes and microstructures of the obtained TNHs are further examined by field-emission scanning electron microscopy (FE-SEM) and transmission electron microscopy (TEM). Fig. 1A shows the FE-SEM image of the PPy–PMo_{12}/rGO TNHs. In contrast to pure rGO (Fig. S3A and B, ESI†) and PPy/rGO (Fig. S3C and D, ESI†), the obvious re-stacking of rGO nanosheets disappears, and large-area thicker sheet-like structures with rough surfaces and curled edges can be observed. This transformation is attributed to the intercalation and polymerization of Py on the surfaces of the initial GO decorated with PMo_{12}, leading to exfoliation and reduction of GO to rGO by HPB that restores PMo_{12} between the interfaces of PPy and rGO. Besides, the PPy–PMo_{12} nanoparticles are uniformly coated on the rGO sheet, generating many mesopores on the surface of the nanohybrids. The corresponding TEM analysis (Fig. 1B) further confirms the successful integration of PPy–PMo_{12} onto rGO to form fish scale-like TNHs. The average size of PPy–PMo_{12} particles is about 65 nm, and the mesopores on each TNH can be clearly observed. Related N_2 adsorption–desorption tests further confirm the existence of mesopores in the obtained TNHs (Fig. S4, ESI†). The average pore diameter is about 2–10 nm. Compared with that of PPy/rGO, the relatively larger and broader pore size distribution of PPy–PMo_{12}/rGO TNHs may facilitate the intercalation and deintercalation of electrolyte ions, which is beneficial to improve the energy storage performance.

The electrochemical properties of PPy–PMo_{12}/rGO TNHs are firstly evaluated in three electrode systems using 0.5 M H_2SO_4 solution as the electrolyte. Fig. 2A shows the representative cyclic voltammetry (CV) curves of PPy–PMo_{12}/rGO TNHs, PPy/rGO and pure rGO in the range of −0.2 to 0.8 V (*vs.* Ag/AgCl) with a scan rate of 50 mV s^{-1}. For pure rGO, only a small, rectangular CV plot is observed, indicating the obvious electron double layer capacitance feature. In the presence of PPy, a large and nearly rectangular CV plot without distinct redox peaks is
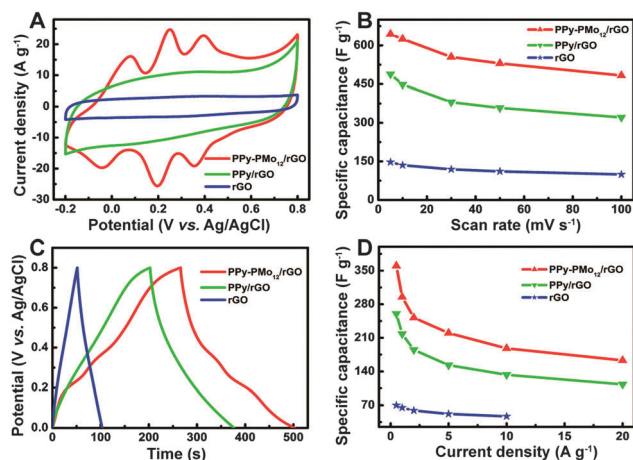

Scheme 1 The schematic diagram for formation of PPy–PMo_{12}/rGO TNHs.

Fig. 2 (A) CV curves for PPy–PMo$_{12}$/rGO TNHs, PPy/rGO, and rGO in 0.5 M H$_2$SO$_4$ solution at a scan rate of 50 mV s^{-1}. (B) Specific capacitances *versus* scan rate plots. (C) Galvanostatic charge–discharge plots at a current density of 1 A g^{-1}. (D) Specific capacitances of PPy–PMo$_{12}$/rGO TNHs, PPy/rGO, and rGO at various current densities.
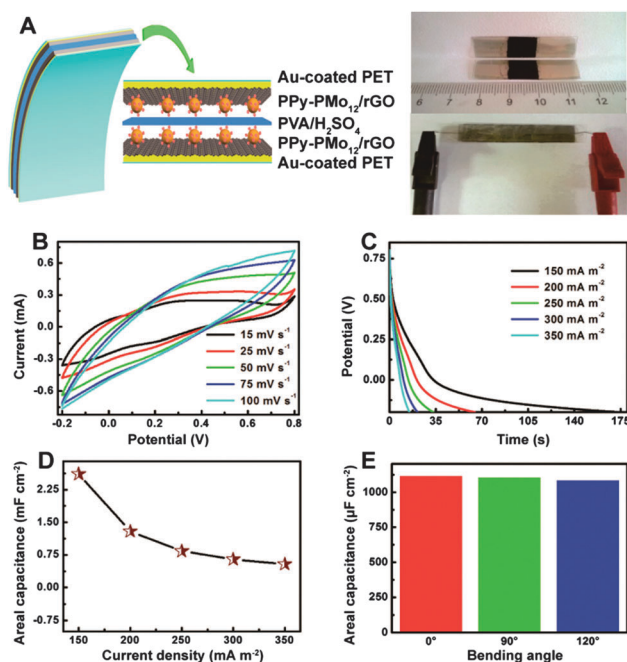

Fig. 3 (A) Schematic diagrams (left) of the PPG-SSCs and photographs (right) of the two electrodes for the PPG-SSCs. (B) CV curves of PPG-SSCs measured at different scan rates. (C) Discharge branch curves of the PPG-SSC device. (D) Areal specific capacitances of the device at various current densities. (E) Specific capacitances of the device by bending at different angles.

observed for the PPy/rGO due to partial pseudo-capacitance contribution from PPy. For the PPy–PMo$_{12}$/rGO TNHs, a much larger CV plot and three pairs of reversible redox peaks corresponding to the reduction–oxidation of PMo$_{12}$ anions are clearly observed,[30] implying the coexistence of the electron double layer and obvious pseudo-capacitance. With the increase of scan rate, the appearances of the CV plots for PPy–PMo$_{12}$/rGO TNHs are nearly unchanged, but their peak currents increase accordingly (Fig. S5, ESI†), indicating that the TNHs are beneficial for fast redox reactions. Based on the CV plots for different scan rates, the specific capacitances of the PPy–PMo$_{12}$/rGO TNHs, PPy/rGO and pure rGO electrodes can be calculated. The related specific capacitances *versus* the scan rate plots are shown in Fig. 2B. Obviously, compared with pure rGO and PPy/rGO, the introduction of PMo$_{12}$ significantly improves the specific capacitance of the TNH electrode. To further evaluate the potential application of the TNHs as an electrode for electrochemical SCs, galvanostatic charge–discharge tests are conducted at various current densities (from 0.5 to 20 A g^{-1}) (Fig. S5, ESI†). For comparison, Fig. 2C gives the related galvanostatic charge–discharge plots for the TNHs, PPy/rGO and pure rGO at a current density of 1 A g^{-1}. Calculated from the discharge branches, the mass specific capacitances of the TNH electrode (Fig. 2D) are 360, 295, 252, 220, 188, and 163 F g^{-1} at the current densities of 0.5, 1, 2, 5, 10, and 20 A g^{-1}, respectively, which are much higher than those of PPy/GO or G,[31,32] and rGO–PMo$_{12}$ hybrids.[33] Moreover, at the same current density, the specific capacitance of the TNHs is superior to that of pure rGO and PPy/rGO, revealing that the components and microstructures greatly affect the energy storage capacity. Table S1 (ESI†) shows the comparison of specific capacitance of PPy–PMo$_{12}$/rGO TNHs with the reported graphene and POM-based composite materials.

To develop a flexible power source, the stacked symmetric all-solid-state SCs are further fabricated using PPy–PMo$_{12}$/rGO as the active material, which is marked as PPG-SSCs. The PVA/H$_2$SO$_4$

gel serves both as the separator and as the solid electrolyte. The detailed configuration of PPG-SSCs is shown in Fig. 3A. The working area of the device is about 1.0 cm^2. The capacitive behaviours of the solid device are first studied by CV in the range of −0.2 to 0.8 V with the scan rates ranging from 15 to 100 mV s^{-1} (Fig. 3B). The CV plots are symmetrical and deviate from a rectangular shape due to the surface electro-sorption of H$^+$ and the consecutive reversible surface redox reactions of PMo$_{12}$ and PPy by H$^+$ intercalation/deintercalation. The absence of redox peaks implies the device charged and discharged at a pseudo-constant rate during the voltammetric cycles.[34] To further evaluate its energy storage performance, galvanostatic charge–discharge tests are performed. Unlike previous reports that pursue energy storage at low current densities,[35] we perform charge–discharge tests at relatively high current densities from 150 to 350 mA m^{-2}. From the discharge branch plots (Fig. 3C), the areal specific capacitances of the device are calculated to be 2.61, 1.29, 0.84, 0.65, and 0.54 mF cm^{-2} at the current densities of 150, 200, 250, 300, and 350 mA m^{-2} respectively (Fig. 3D), which are superior to G (394 μF cm^{-2}),[36] 2D SnSe$_2$ nanodisk (250 μF cm^{-2}) and SnSe nanosheet (442 μF cm^{-2}) based solid devices.[37]

These results reveal that the PPG-SSC device exhibits excellent energy storage performance even at very high current densities. In addition, the bending tests of the device at various angles are further executed and the electrochemical responses are recorded accordingly (Fig. S6, ESI†). The nearly identical electrochemical signals confirm that the device's flexibility and mechanical stability are excellent (Fig. 3E). Moreover, the durability tests reveal that the device also has good cycling stability (Fig. S7, ESI†).

In summary, novel PPy–PMo$_{12}$/rGO TNHs have been synthesized *via* a PMo$_{12}$-mediated one-pot redox relay strategy. In the TNHs, the PPy–PMo$_{12}$ nanoparticles with a size of about 65 nm are well anchored on rGO nanosheets, which not only inhibit the re-stacking of rGO and contribute to pseudo-capacitance but also create many mesopores that are helpful for ion diffusion and electron transport. As a result, the TNHs exhibit excellent supercapacitive performance in a 0.5 M H$_2$SO$_4$ solution. Thus, using those TNHs as active material, the flexible, all-solid-state SCs, marked as PPG-SSCs, are further fabricated with the dream to develop flexible power sources. At the current density of 150 mA m^{-2}, the areal specific capacitance of the PPG-SSCs device reaches 2.61 mF cm^{-2}, which is much higher than those of G, 2D SnSe$_2$ and SnSe based solid devices. Also, the PPG-SSC device exhibits excellent flexibility and mechanical stability, good rate capability and cycling performance, showing promise as a flexible power supply for driving small nanoelectronic devices in integrated nanosystems. This work not only enriches the current hybrid electrode family and provides an ideal candidate for flexible SSCs but also paves the way for future designing advanced nanohybrids to use in flexible wearable electronics, energy storage, and sensing devices.

Notes and references

1 J. R. Miller and P. Simon, *Science*, 2008, **321**, 651.
2 C. Liu, F. Li, L. P. Ma and H. M. Cheng, *Adv. Mater.*, 2010, **22**, E28.
3 V. Augustyn, P. Simon and B. Dunn, *Energy Environ. Sci.*, 2014, **7**, 1597.
4 K. M. Hercule, Q. Wei, A. M. Khan, Y. Zhao, X. Tian and L. Mai, *Nano Lett.*, 2013, **13**, 5685.
5 H. Cong, X. Ren, P. Wang and S. Yu, *Energy Environ. Sci.*, 2013, **6**, 1185.
6 Z. Liu, J. Xu, D. Chen and G. Shen, *Chem. Soc. Rev.*, 2015, **44**, 161.
7 J. Yan, Q. Wang, T. Wei and Z. Fan, *Adv. Energy Mater.*, 2014, **4**, 1300816.
8 J. Ren, W. Bai, G. Guan, Y. Zhang and H. Peng, *Adv. Mater.*, 2013, **25**, 5965.
9 Z. Cao and B. Wei, *Energy Environ. Sci.*, 2013, **6**, 3183.
10 Y. Xu, Z. Lin, X. Zhong, X. Huang, N. O. Weiss, Y. Huang and X. Duan, *Nat. Commun.*, 2014, **5**, 4554.
11 C. Guan, X. L. Li, Z. L. Wang, X. H. Cao, C. Soci, H. Zhang and H. J. Fan, *Adv. Mater.*, 2012, **24**, 4186.
12 S. Gao, Y. Sun, F. Lei, L. Liang, J. Liu, W. Bi, B. Pan and Y. Xie, *Angew. Chem., Int. Ed.*, 2014, **53**, 12789.
13 Y. Yang, H. Fei, G. Ruan, C. Xiang and J. M. Tour, *Adv. Mater.*, 2014, **26**, 8163.
14 M. R. Arcila-Velez and M. E. Roberts, *Chem. Mater.*, 2014, **26**, 1601.
15 Y. Sun, Q. Wu and G. Shi, *Energy Environ. Sci.*, 2011, **4**, 1113.
16 J. Zhu, D. Yang, Z. Yin, Q. Yan and H. Zhang, *Small*, 2014, **10**, 3480.
17 X. Yu, B. Lu and Z. Xu, *Adv. Mater.*, 2014, **26**, 1044.
18 J. Xie, X. Sun, N. Zhang, K. Xu, M. Zhou and Y. Xie, *Nano Energy*, 2013, **2**, 65.
19 L. Peng, X. Peng, B. Liu, C. Wu, Y. Xie and G. Yu, *Nano Lett.*, 2013, **13**, 2151.
20 M. Xue, F. Li, J. Zhu, H. Song, M. Zhang and T. Cao, *Adv. Funct. Mater.*, 2012, **22**, 1284.
21 L. Wang, Y. Ye, X. Lu, Z. Wen, Z. Li, H. Hou and Y. Song, *Sci. Rep.*, 2013, **3**, 3568.
22 H. Fan, N. Zhao, H. Wang, J. Xu and F. Pan, *J. Mater. Chem. A*, 2014, **2**, 12340.
23 Y. Hou, Y. Cheng, T. Hobson and J. Liu, *Nano Lett.*, 2010, **10**, 2727.
24 L. Qie, W. Chen, H. Xu, X. Xiong, Y. Jiang, F. Zou, X. Hu, Y. Xin, Z. Zhang and Y. Huang, *Energy Environ. Sci.*, 2013, **6**, 2497.
25 J. Wang, Y. Xu, F. Yan, J. Zhu and J. Wang, *J. Power Sources*, 2011, **196**, 2373.
26 Z. Cui, C. X. Guo, W. Yuan and C. Li, *Phys. Chem. Chem. Phys.*, 2012, **14**, 12823.
27 M. Jiang, D. Zhu, H. Zhang and X. Zhao, *New J. Chem.*, 2014, **38**, 3354.
28 P. Gómez-Romero and M. Lira-Cantú, *Adv. Mater.*, 1997, **9**, 144.
29 H. Li, S. Pang, X. Feng, K. Müllen and C. Bubeck, *Chem. Commun.*, 2010, **46**, 6243.
30 M. Sadakane and E. Steckhan, *Chem. Rev.*, 1998, **98**, 219.
31 J. Zhang and X. S. Zhao, *J. Phys. Chem. C*, 2012, **116**, 5420.
32 J. Zhang, P. Chen, B. H. Oh and M. B. Chan-Park, *Nanoscale*, 2013, **5**, 9860.
33 J. Suarez-Guevara, V. Ruiz and P. Gomez-Romero, *Phys. Chem. Chem. Phys.*, 2014, **16**, 20411.
34 X. Lang, A. Hirata, T. Fujita and M. Chen, *Nat. Nanotechnol.*, 2011, **6**, 232.
35 P. Simon, Y. Gogotsi and B. Dunn, *Science*, 2014, **343**, 1210.
36 J. J. Yoo, K. Balakrishnan, J. Huang, V. Meunier, B. G. Sumpter, A. Srivastava, M. Conway, A. L. Reddy, J. Yu, R. Vajtai and P. M. Ajayan, *Nano Lett.*, 2011, **11**, 1423.
37 C. Zhang, H. Yin, M. Han, Z. Dai, H. Pang, Y. Zheng, Y. Lan, J. Bao and J. Zhu, *ACS Nano*, 2014, **8**, 3761.